AAAS
Research
Volume 2020, Article ID 4093732, 12 pages
https://doi.org/10.34133/2020/4093732

Research
A SCIENCE PARTNER JOURNAL

Research Article

3D Shapeable, Superior Electrically Conductive Cellulose Nanofibers/$Ti_3C_2T_x$ MXene Aerogels/Epoxy Nanocomposites for Promising EMI Shielding

Lei Wang,[1] **Ping Song**,[1] **Cheng-Te Lin**,[2] **Jie Kong**,[1] **and Junwei Gu**[1]

[1]*Shaanxi Key Laboratory of Macromolecular Science and Technology, School of Chemistry and Chemical Engineering, Northwestern Polytechnical University, Xi'an, Shaanxi 710072, China*
[2]*Key Laboratory of Marine Materials and Related Technologies, Zhejiang Key Laboratory of Marine Materials and Protective Technologies, Ningbo Institute of Materials Technology and Engineering (NIMTE), Chinese Academy of Sciences, Ningbo 315201, China*

Correspondence should be addressed to Junwei Gu; gjw@nwpu.edu.cn

Received 20 March 2020; Accepted 8 May 2020; Published 17 June 2020

In this work, 3D highly electrically conductive cellulose nanofibers (CNF)/$Ti_3C_2T_x$ MXene aerogels (CTA) with aligned porous structures are fabricated by directional freezing followed by freeze-drying technique, and the thermally annealed CTA (TCTA)/epoxy nanocomposites are then fabricated by thermal annealing of CTA, subsequent vacuum-assisted impregnation and curing method. Results show that TCTA/epoxy nanocomposites possess 3D highly conductive networks with ultralow percolation threshold of 0.20 vol% $Ti_3C_2T_x$. When the volume fraction of $Ti_3C_2T_x$ is 1.38 vol%, the electrical conductivity (σ), electromagnetic interference shielding effectiveness (EMI SE), and SE divided by thickness (SE/d) values of the TCTA/epoxy nanocomposites reach 1672 S m^{-1}, 74 dB, and 37 dB mm^{-1}, respectively, which are almost the highest values compared to those of polymer nanocomposites reported previously at the same filler content. In addition, compared to those of the samples without $Ti_3C_2T_x$, the storage modulus and heat-resistance index of TCTA/epoxy nanocomposites are enhanced to 9792.5 MPa and 310.7°C, increased by 62% and 6.9°C, respectively, presenting outstanding mechanical properties and thermal stabilities. The fabricated lightweight, easy-to-process, and shapeable TCTA/epoxy nanocomposites with superior EMI SE values, excellent mechanical properties, and thermal stabilities greatly broaden the applications of MXene-based polymer composites in the field of EMI shielding.

1. Introduction

With the rapid development of modern electronic information technology, especially the aerospace weapons and equipment technology, electromagnetic interference (EMI) pollution caused by high-frequency and high-power electronic equipment is becoming more and more severe, and the request for EMI shielding performances of existing materials in service becomes increasingly demanding [1–4]. Investigations on the EMI shielding materials with low density, excellent mechanical properties, and remarkable shielding effectiveness (SE), especially, ease of large-scale and complex structure production, are of great significance for the development and upgrading of aerospace weapons and equipment.

Nowadays, conductive polymer nanocomposites are increasingly favored in the field of EMI shielding due to their high specific strength, adjustable properties, and excellent chemical stability [5–8]. Generally, it is necessary to add a large amount of conductive fillers to achieve the required EMI SE value (20 dB for commercial application), which usually causes processing difficulties and poor mechanical properties [9, 10]. In order to overcome this issue, researchers have attempted to further improve EMI SE values of the polymer composites by functionalized conductive fillers or microstructural regulation of the fillers. Eswaraiah et al. improved the dispersion of graphene in polyvinylidene fluoride (PVDF) by surface prefunctionalization of graphene sheets, and the EMI SE value of 7 wt% functionalized graphene/PVDF was up to 26 dB [11]. Yousefi et al. prepared

graphene/epoxy nanocomposites by solution casting method, and the graphene/epoxy nanocomposites exhibited EMI SE value of 38 dB with a loading of 3 wt% graphene [12]. In our previous work, the EMI SE value of 35 wt% 3D graphene nanoplatelets/polystyrene (GNPs/PS) prepared by electrospinning method reached 33 dB, which was improved by 106% compared to that (16 dB) of randomly dispersed GNPs/PS at the same loading of GNPs [13]. The above methods can improve the possibility for the formation of conductive networks or decrease percolation threshold of conductive fillers. However, the improvement effect is limited based on the abovementioned methods, and it still demands a large amount of conductive fillers to achieve ideal EMI SE.

Construction of 3D conductive networks has proven to be an effective way to remarkably improve EMI SE values at low filler loading [14–17]. Chen et al. prepared carbon nanotube foam/epoxy nanocomposites by chemical vapor deposition (CVD) method. When the carbon nanotube foam was only 0.66 wt%, the EMI SE value of the nanocomposites was 33 dB, which was 10 times higher than that of the counterpart (0.66 wt%) prepared by blend-casting method, due to the formation of 3D highly conductive networks of carbon nanotube foam [18]. Sun et al. reported that PS@$Ti_3C_2T_x$ nanocomposites fabricated by electrostatic self-assembly and molding method also demonstrated excellent EMI SE values, because of the contribution of 3D highly conductive networks embedded with the matrix [19]. With only 4.0 wt% $Ti_3C_2T_x$, the electrical conductivity (σ) and EMI SE value of PS@$Ti_3C_2T_x$ nanocomposites reached 1081 S m^{-1} and 54 dB, respectively. Although the EMI SE values based on 3D conductive networks are greatly increased compared to those of the composites prepared by blend-casting method with randomly oriented filler microstructure, they have the similar problems including energy-consuming, limited sample sizes, and uncontrollable shape. Recently, the porous foams made from the assembly of conductive fillers with the aid of polymers, such as cellulose nanofibers (CNF), polyvinyl alcohol (PVA), and polyetherimide (PEI), have been reported [20–25]. Ling et al. [26] prepared graphene/PEI hybrid foams with a pore size of 9-16 μm by solvent evaporation, showing an adjustable EMI SE value between 3 and 13 dB by controlling the loading of graphene. Xu et al. prepared porous PVA/$Ti_3C_2T_x$ hybrid foams with different thicknesses by freeze-drying and molding method after self-assembly of a mixture of PVA and $Ti_3C_2T_x$ and realized the variable EMI SE values of 26-33 dB [27].

Although the 3D conductive networks with randomly distributed microstructure can significantly reduce the amount of conductive fillers and improve σ values, it still fails to make full use of conductive fillers to block electromagnetic waves. Compared to 3D conductive networks with isotropic orientation, aligned conductive networks can not only further reduce the percolation threshold of conductive fillers but also promote efficient utilization of filler/polymer interface, thus enhancing the multiple reflection and reabsorption of electromagnetic waves between aligned fillers and finally improving the attenuation of electromagnetic waves. Some techniques have been developed for the creation of aligned conductive networks, including template-derived method, directional freezing, and 3D printing process [28–30]. Compared to other methods, directional freezing is a simple, practical, and widely used method, which can be carried out in aqueous environment and easy to design the resulting structure. Li et al. prepared anisotropic graphene aerogel/epoxy nanocomposites with EMI SE value of 32 dB along axial direction by directional freezing and freeze-drying. Compared to conventional graphene aerogels (27 dB), EMI SE value of the nanocomposites was increased by 18.5% with 0.8 wt% graphene loading [31]. Zeng et al. reported 7.2 wt% anisotropic multiwalled carbon nanotubes (MWCNT)/waterborne polyurethane (WPU) foams with EMI SE value up to 50 dB along axial direction by directional freezing [32]. However, except graphene, so far the polymer nanocomposites with aligned conductive networks using other 2D materials, such as MXene ($Ti_3C_2T_x$), have seldom been reported yet.

As a degradable nanomaterial with abundant source, CNF is a promising green material owing to its good biocompatibility, excellent mechanical properties, and low density and has broad application prospects in EMI shielding, energy storage, battery applications, etc. [33–36]. In this work, CNF is assembled with $Ti_3C_2T_x$ nanosheets by hydrogen bonding, followed by directional freezing and freeze-drying technique, in order to obtain the CNF/$Ti_3C_2T_x$ aerogel (CTA). The thermally annealed CTA (TCTA)/epoxy nanocomposites are then fabricated by thermal annealing of CTA, subsequent vacuum-assisted impregnation and curing method. The morphology and chemical compositions of $Ti_3C_2T_x$ nanosheets and TCTA are characterized by scanning electron microscopy (SEM), X-ray diffraction (XRD), Raman spectroscopy, and X-ray photoelectron spectroscopy (XPS). Furthermore, the effect of the volume fraction of $Ti_3C_2T_x$ nanosheets on σ, EMI SE values, mechanical properties, and thermal stabilities of TCTA/epoxy nanocomposites is investigated, and the mechanism of EMI SE improvement of the nanocomposites is also proposed.

2. Results

Figure 1(a) illustrates the schematic diagram of the fabrication of TCTA/epoxy nanocomposites. The $Ti_3C_2T_x$ nanosheets are exfoliated by ion intercalation method and assembled with CNF by directional freezing and freeze-drying technique, followed by annealing to decrease the density and improve σ. Finally, the TCTA/epoxy nanocomposites are prepared by impregnation with epoxy resins. As indicated in Figure 1(b), CNF and $Ti_3C_2T_x$ nanosheets overlap with each other by hydrogen bonding, which effectively prevents the agglomeration of $Ti_3C_2T_x$ nanosheets. In Figure 1(c), TCTA with various complex shapes can be prepared *via* different molds, indicating that our proposed method can satisfy the fabrication of various complex structures with large-scale production.

Figure 2 shows the structural and morphological characterizations of $Ti_3C_2T_x$ nanosheets. In Figure 2(a), the (002) diffraction peak shifts from 9.7° for Ti_3AlC_2 to 6.2° for $Ti_3C_2T_x$, indicating that the corresponding interlayer spacing

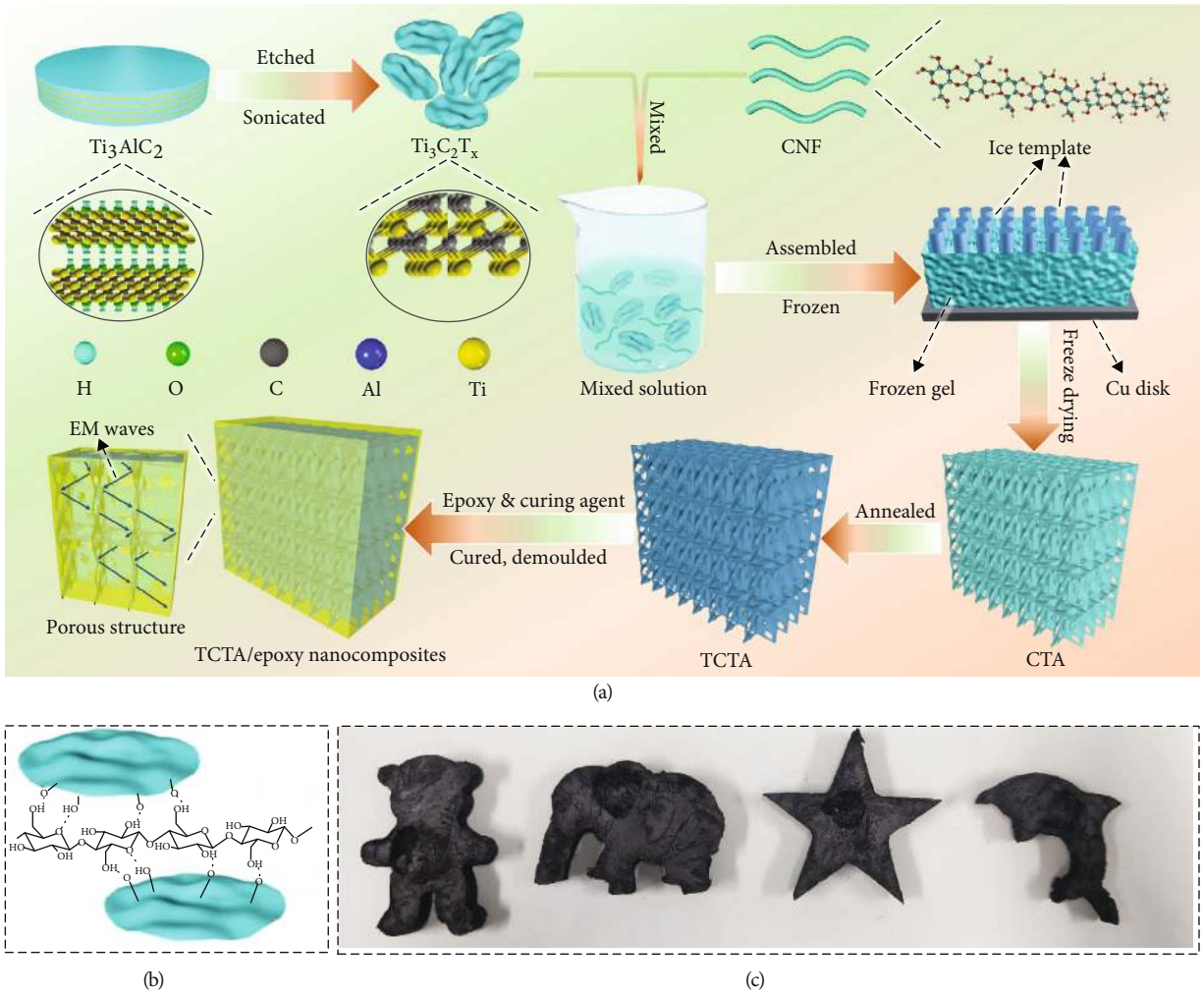

Figure 1: (a) Schematic illustration of fabrication for TCTA/epoxy nanocomposites. (b) Schematic illustration of the interaction between CNF and $Ti_3C_2T_x$. (c) Digital images for various shapes of TCTA showing plasticity and machinability.

is enlarged from 1.10 to 1.42 nm, due to the removal of Al atomic layers, proving the successful synthesis of $Ti_3C_2T_x$ nanosheets [37, 38]. In the wide-scan XPS spectra (Figure S1(b)), the Al 2s and Al 2p peaks of Ti_3AlC_2 disappear after etching, while the new peaks of O 1s and F 1s are observed in $Ti_3C_2T_x$ [39], confirming the complete removal of Al atomic layer and the formation of -OH and -F groups on the surface of $Ti_3C_2T_x$ nanosheets. In Figure S1(d), the absorption peaks at 3460, 1630, and 600 cm^{-1} of $Ti_3C_2T_x$ nanosheets are ascribed to the stretching vibration from -OH, C=O, and Ti-O groups, respectively [40, 41]. In contrast to the dense-layered structures of Ti_3AlC_2 raw material in Figure 2(b) and Figure S1(a), after etching, $Ti_3C_2T_x$ nanosheets exhibit typical 2D structure with uniform thickness and a lateral size of about 800 nm, as shown in Figure 2(c). Typical Tyndall effect appears in diluted $Ti_3C_2T_x$ suspension in Figure 2(d), proving that the hydrophilic functional groups render the surface of $Ti_3C_2T_x$ nanosheets to form a stable suspension. In Figure 2(e) and Figure S1(c), TEM and AFM images of $Ti_3C_2T_x$ nanosheets indicate that the $Ti_3C_2T_x$ nanosheets are ultrathin with an average thickness of 2.04 nm and highly transparent under electron irradiation, in which the surface of $Ti_3C_2T_x$ nanosheets is clear without any impurity and byproduct. In addition, the selected-area electron diffraction (SEAD) pattern image (Figure 2(e′)) reveals the typical hexagonal structure of $Ti_3C_2T_x$ nanosheets [42]. All the results demonstrate the successful synthesis of $Ti_3C_2T_x$ nanosheets with good crystallinity and clean surface.

Figures 3(b)–3(g) present the SEM images of TCTA-(1-6) prepared by directional freeze-drying process using $Ti_3C_2T_x$ nanosheets and CNF, in which $Ti_3C_2T_x$ and CNF support each other, thus preventing agglomeration of each component and promoting the formation of aligned porous structures which would not be altered after annealing. In contrast, TCTA-0 exhibits a dense porous structure with random orientation based on the intertwining of CNF (Figures 3(a) and S2). As shown in Figures 3(h) and S3, with increasing volume fraction of $Ti_3C_2T_x$ nanosheets, the cell density of TCTA monotonically increases and the cell size correspondingly decreases from 21.3 μm (TCTA-1) to 10.2 μm (TCTA-6). The aligned porous structures can be

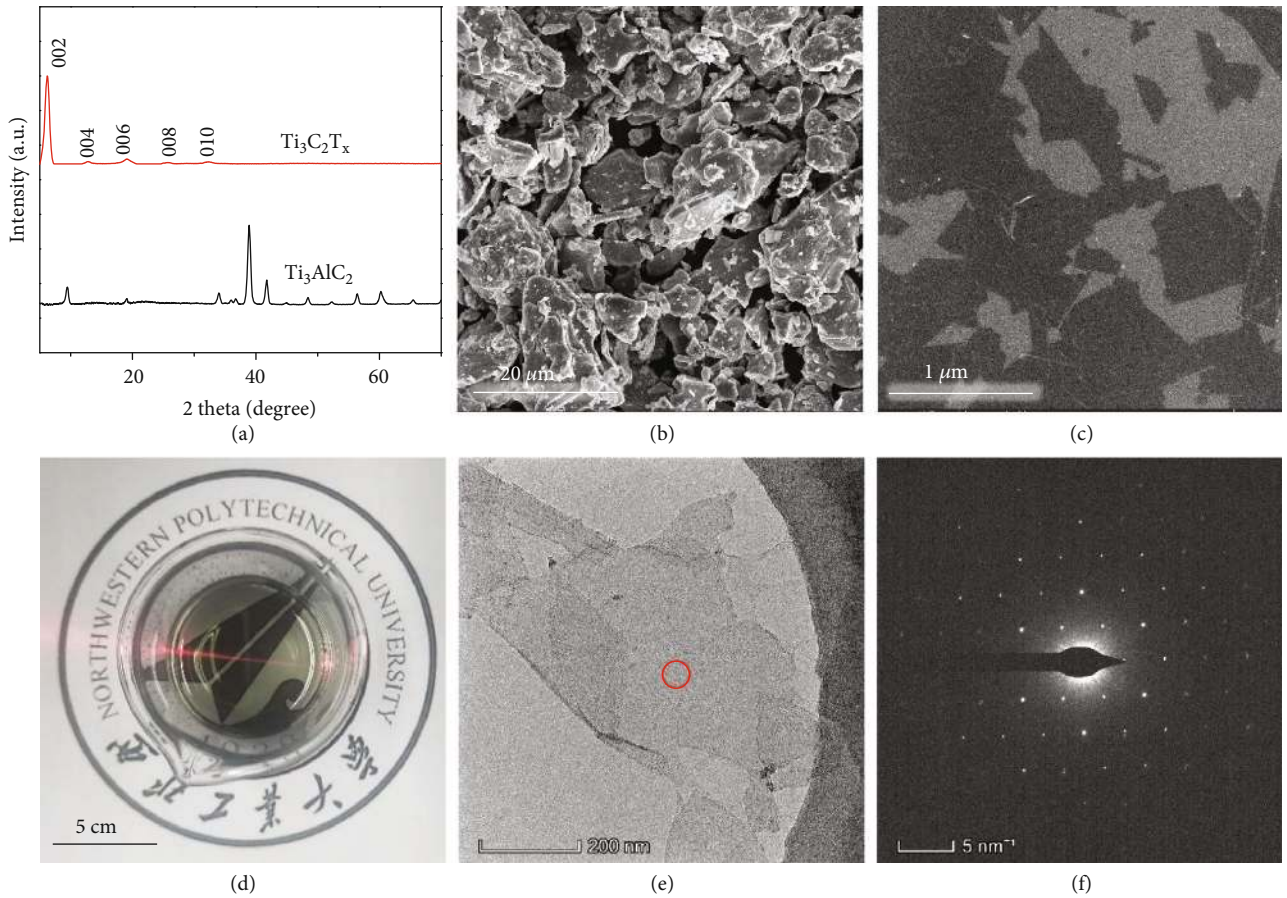

FIGURE 2: (a) XRD pattern for Ti_3AlC_2 and $Ti_3C_2T_x$. SEM images of (b) Ti_3AlC_2 and (c) $Ti_3C_2T_x$ nanosheets. (d) Tyndall effect of diluted $Ti_3C_2T_x$ suspension using a laser pointer. (e) TEM image and (e′) SEAD pattern of $Ti_3C_2T_x$ nanosheets.

attributed to the fact that ice crystals grow from the bottom to the top of the samples during directional freezing process, by which $Ti_3C_2T_x$ and CNF are forced to align along the growth direction of ice crystals, resulting in the formation of highly aligned microstructure after freeze-drying. And the cell size decreases with an increase of volume fraction of $Ti_3C_2T_x$ which is attributed to the increased nucleation density of active seeds that limits the further growth of ice crystals. In Figure 3(i), the characteristic peaks in the Raman spectra of TCTA for D- and G-bands at 1352 and 1584 cm^{-1}, respectively, are attributed to the residual carbon from decomposed CNF after annealing [43–45]. After incorporation of $Ti_3C_2T_x$, the newly appeared peak at 200 cm^{-1} can be assigned to A1g symmetry out-of-plane vibration of Ti atoms, and the peaks at 374 and 583 cm^{-1} are ascribed to the Eg group vibration and in-plane (shear) modes of Ti, C, and surface functional groups [46]. In Figure S4, there are two peaks ascribed to Ti and F elements in the XPS survey spectrum of TCTA-6 [47] but cannot be seen in the case of TCTA-0. Moreover, compared to the C 1s spectrum of TCTA-0 (Figures 3(j) and 3(k)) (TCTA-6) presents Ti-C (282.3 eV), Ti-C-O (283.2 eV), and C-F (287 eV) bonds due to the incorporation of $Ti_3C_2T_x$ nanosheets. In addition, the ratio of characteristic peaks of C-O and C=O-O still maintains a high level after annealing. It indicates that there are still a large number of polar functional groups attributed to $Ti_3C_2T_x$ and CNF in TCTA-6, such as -OH and –COOH. The characteristic peak of TiO_2 can be observed in the Ti 2p XPS spectrum of TCTA-6 in Figure 3(k′) owing to the weak oxidation of $Ti_3C_2T_x$ (Figure S5) during etching process.

The aerogel sample (TCTA-6) has a lightweight architecture (Figure 4(a)) and excellent mechanical properties to support a 500 g load (1300 times larger than the weight itself (390 mg), see Figure 4(b)), which is based on the well-aligned porous structure and reinforcement of CNF. The sample density ranges from 2.4 mg cm^{-3} (TCTA-0) to 45.0 mg cm^{-3} (TCTA-6), as listed in Table S1. In Figures 4(c)–4(d″), both top and cross-sectional views of TCTA-6 exhibit similar aligned porous structure. In these SEM images, $Ti_3C_2T_x$ nanosheets overlap with each other to form rigid and long-range aligned cell walls, giving TCTA-6 an outstanding mechanical property to resist compression, and the cells composed of $Ti_3C_2T_x$ nanosheets can serve as a buffer against stress.

The electrical conductivities (σ) and EMI SE values of TCTA and corresponding nanocomposites were investigated as the results shown in Figure 5. In Figures 5(a) and S6(a) and Tables S1 and S2, the σ values of TCTA increase rapidly from 0.0186 S m^{-1} to 1992 S m^{-1} for TCTA-0 and TCTA-6, respectively, and the corresponding σ values of the

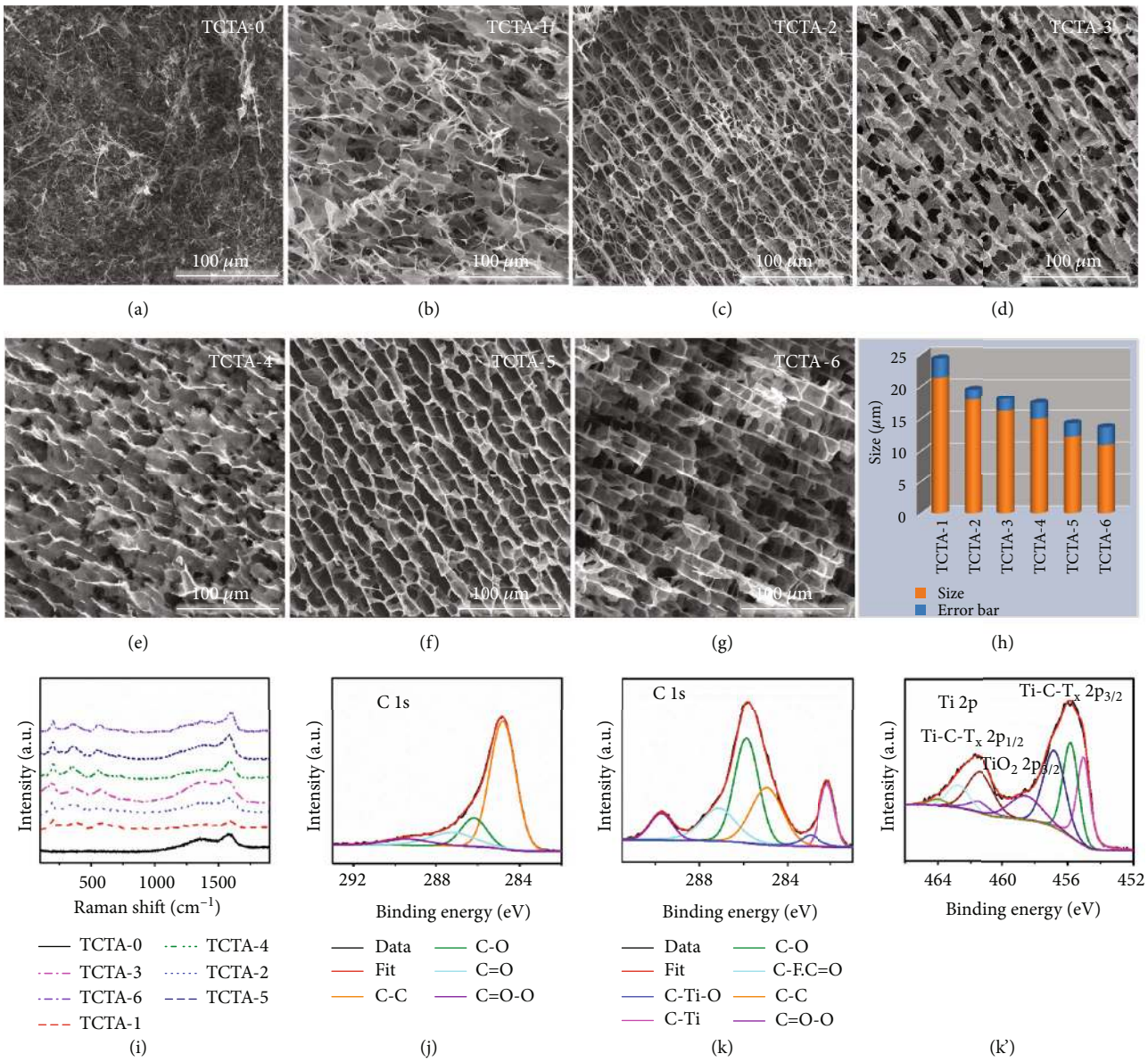

FIGURE 3: (a–g) SEM images of TCTA. (h) Comparison of average cell sizes for TCTA. (i) Raman spectra of TCTA. (j) C 1s spectra of TCTA-0. (k) C 1s and (k′) Ti 2p spectra of TCTA-6.

nanocomposites increase from 8.6×10^{-3} S m^{-1} to 1672 S m^{-1} for TCTA-0/ and TCTA-6/epoxy nanocomposites with 1.38 vol% $Ti_3C_2T_x$ addition, respectively. As the volume fraction of $Ti_3C_2T_x$ increases, the contact possibility between $Ti_3C_2T_x$ nanosheets with excellent electrical conductivity increases within the matrix, resulting in the formation of 3D conductive networks in TCTA/epoxy nanocomposites with excellent σ values [48]. The TCTA-6/epoxy nanocomposites present anisotropic electrical conductivity, which is 1672 S m^{-1} along the axial direction and 1283 S m^{-1} along the radial direction (see Figure S6(b)). Our results exhibit that the σ values of TCTA/epoxy nanocomposites are in accordance with the power law equation:

$$\sigma = \sigma_0[(\rho - \rho_c)(1 - \rho_c)]^t, \quad (1)$$

where σ_0 is a constant dependent on the intrinsic conductivity of $Ti_3C_2T_x$ nanosheets, ρ_c is the volume fraction of $Ti_3C_2T_x$ at percolation threshold, and t is the critical exponent reflecting the dimensionality of the nanocomposites. The fitting results show the percolation threshold is 0.20 vol% of $Ti_3C_2T_x$ (Figure 5(a)), which is much lower than 1.70 vol% in $Ti_3C_2T_x$/PAM [49], 0.60 vol% in rGO/PVA [50], and also slightly lower than 0.26 vol% in PS@$Ti_3C_2T_x$ [19]. Moreover, the σ value (1672 S m^{-1}) of TCTA/epoxy nanocomposites is almost the highest value in comparison with previously reported polymer composites with conductive fillers such as $Ti_3C_2T_x$, graphene, and carbon nanotubes, at the same filler content [51, 52]. The obtained σ value is also obviously higher than that of recently reported 3D graphene/$Ti_3C_2T_x$ aerogel/epoxy nanocomposite (695.9 S m^{-1}) at 0.99 vol% graphene/$Ti_3C_2T_x$ content [52] and that of

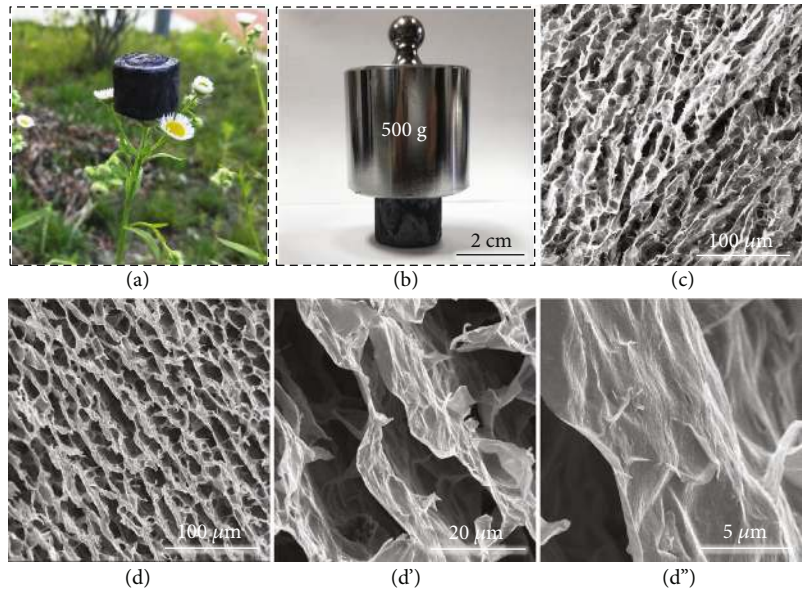

Figure 4: (a) Digital images of TCTA-6 standing on a flower and (b) supporting a load of 500 g. (c) Top view and (d-d″) side view SEM images of TCTA-6.

PS@rGO (1083 S m^{-1}) at 4.80 vol% rGO content [53]. The above results indicate that highly conductive $Ti_3C_2T_x$ and developed conductive networks endow TCTA/epoxy nanocomposites with efficient electron transportation capability, thus presenting remarkable σ values.

Figure 5(b) illustrates EMI SE values of TCTA/epoxy nanocomposites at X-band. The EMI SE value of the nanocomposites without $Ti_3C_2T_x$ addition (TCTA-0) is only 7 dB. After incorporation of $Ti_3C_2T_x$, the EMI SE value of TCTA-1/epoxy nanocomposites at 0.13 vol% $Ti_3C_2T_x$ content rises rapidly to 22 dB (commercial requirement: 20 dB). When the volume fraction of $Ti_3C_2T_x$ is 1.38 vol%, the EMI SE value of TCTA-6/epoxy nanocomposites approaches 74 dB, which is slightly lower than that of TCTA-6 without epoxy matrix (Figure S8(a)), but significantly higher than that of the nanocomposites prepared by blend-casting method with the same volume fraction of $Ti_3C_2T_x$ (19 dB), as displayed in Figure S8(b). In addition, the EMI SE value of TCTA-6/epoxy nanocomposites along the radial direction (74 dB) is much higher than that along the axial direction (57 dB, Figure S8(c)), presenting anisotropic EMI shielding behavior. The σ values of TCTA/epoxy nanocomposites increase gradually with increasing volume fraction of $Ti_3C_2T_x$, causing stronger electric loss (eddy current loss) and enhanced EMI shielding performance.

The specimen thickness is another key factor influencing the EMI SE values of TCTA/epoxy nanocomposites. As an example, TCTA-6/epoxy nanocomposites with 1 mm in thickness display EMI SE value of 30 dB (Figure 5(c)), which is rapidly increased to 74 dB for 2 mm thick sample. In order to further highlight the advantages of highly efficient 3D conductive networks of TCTA/epoxy nanocomposites, the EMI SE divided by thickness (SE/d) reported in the literatures are summarized in Figure 5(d) and Table S3 to compare with our results. Some recent works can be seen in Figure 5(d), such as 10 dB mm^{-1} for 1.34 vol% CNT sponge/epoxy nanocomposites [18], 20 dB mm^{-1} for 0.36 vol% graphene aerogel/polydimethylsiloxane (PDMS) [54], and 31 dB mm^{-1} for 1.9 vol% PS@$Ti_3C_2T_x$ [19]. In contrast, our TCTA/epoxy nanocomposites achieve higher SE/d of 28, 32, and 37 dB mm^{-1} at lower loading of $Ti_3C_2T_x$ (0.82, 1.11, and 1.38 vol%), respectively, demonstrating superior EMI shielding performances.

To explore the shielding mechanism of TCTA/epoxy nanocomposites, Figure 5(e) compares the contribution of absorption shielding effectiveness (SE_A) and reflection shielding effectiveness (SE_R) to total shielding effectiveness (SE_T). Consistent with SE_T, SE_A increases dramatically and is much higher than SE_R. This is because the integrity of aligned porous structures of TCTA is well-maintained inner TCTA/epoxy nanocomposites (Figures 6(a)–6(g′)). In the scanning transmission electron microscope (STEM) images of TCTA-6/epoxy nanocomposites (Figures 6(h)–6(h‴)), a large number of $Ti_3C_2T_x$ nanosheets overlap with each other to form hollow-like skeleton structures, which still remain in the TCTA-6/epoxy nanocomposites after impregnating with epoxy resins. $Ti_3C_2T_x$ nanosheets are assembled into the backbone of the porous structures without any individual nanosheets randomly dispersed inner epoxy matrix. It can be seen from the HRTEM image (Figure 6(h′)) that intrinsic structures of $Ti_3C_2T_x$ are not destroyed after impregnating with epoxy resins, and the interlayer spacing maintains 13.9 Å, similar to that of previous XRD (Figure 2(a)) results, indicating that $Ti_3C_2T_x$ is effectively protected by epoxy resin from oxidation. It is especially important to note that, according to the corresponding high-angle annular dark field image (HAADF, Figure 6(i)) and C elemental spectrum (Figure 6(i′)), the interior of the backbone of TCTA-6 is not hollow structures, but the carbon-rich area. Combined

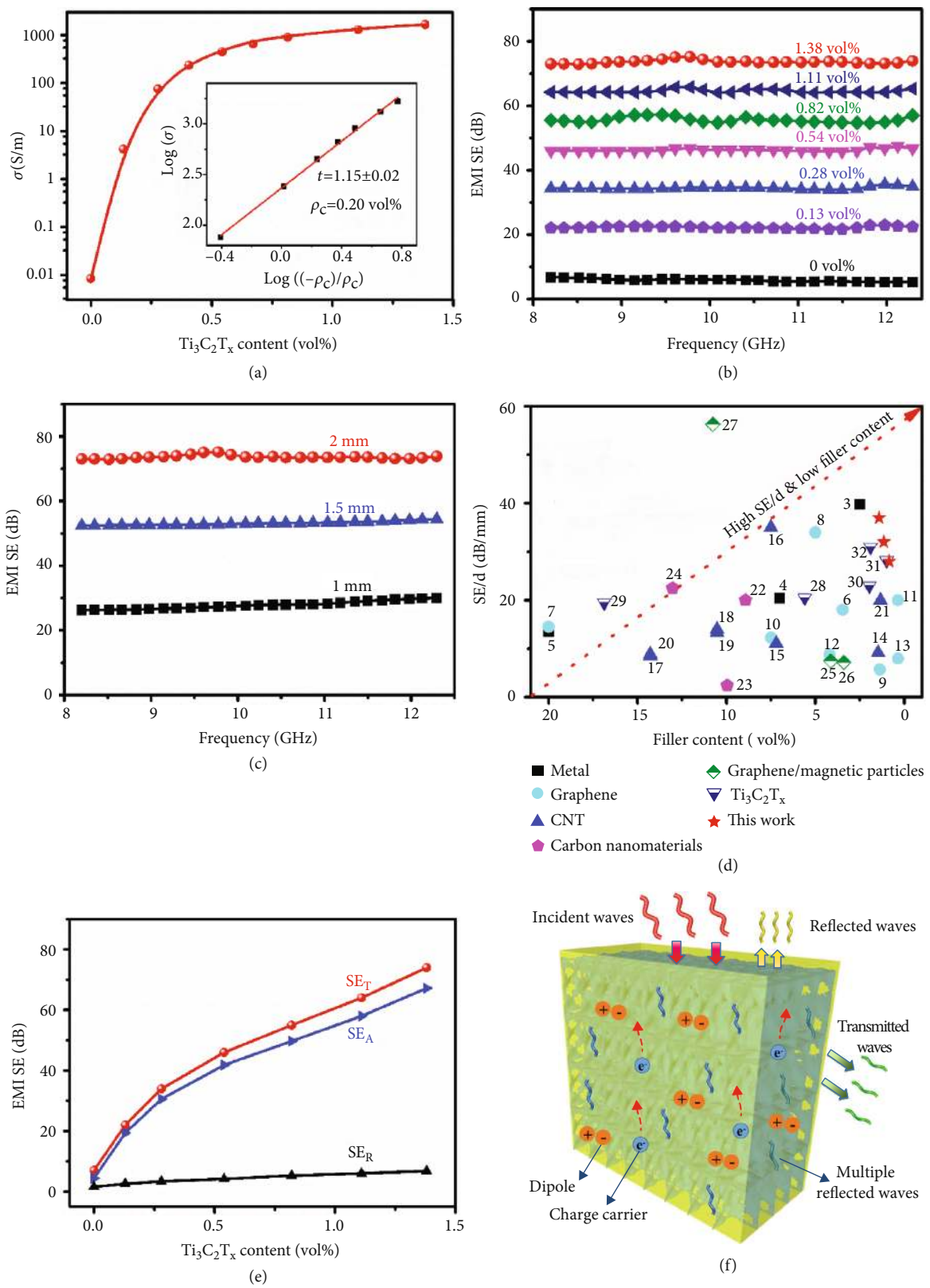

Figure 5: (a) σ values of the TCTA/epoxy nanocomposites. (b) EMI SE values of the TCTA/epoxy nanocomposites at X-band. (c) Thickness *vs.* EMI SE values of the TCTA-6/epoxy nanocomposites. (d) Comparison of EMI SE values for TCTA-6/epoxy nanocomposites (marked as red stars) with those of other reported works. SE/d is depicted as a function of conductive filler volume fraction. Numbers inside the plot correspond to the reference information listed in Table S3. (e) SE_T, SE_A, and SE_R values of the TCTA/epoxy nanocomposites. (f) Schematic diagram of the shielding mechanism for TCTA/epoxy nanocomposites.

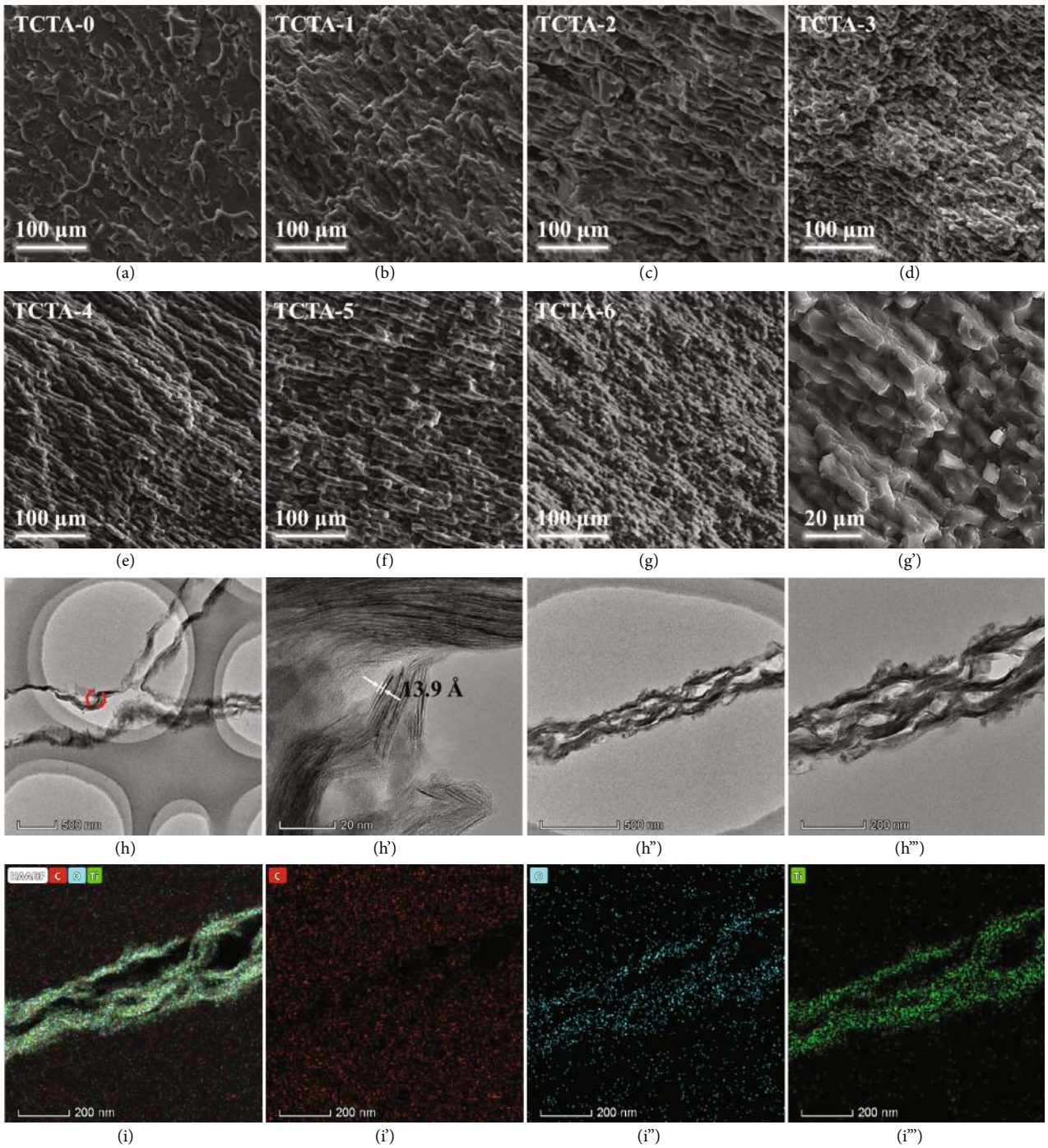

Figure 6: Side view SEM images of the epoxy nanocomposites of (a) TCTA-0, (b) TCTA-1, (c) TCTA-2, (d) TCTA-3, (e) TCTA-4, (f) TCTA-5, (g, g′) TCTA-6, and (h′) HRTEM and (h–h‴) STEM images of the TCTA-6/epoxy nanocomposites and the corresponding (i) HAADF image, elemental mapping images of (i′) C, (i″) O, and (i‴) Ti at the same area.

with the elemental distribution of O and Ti elements (Figures 6(i″) and 6(i‴)) by EDS mapping, it proves that the outer parts of the framework are mainly compactly attached by $Ti_3C_2T_x$ nanosheets, and CNF is encapsulated. This is mainly due to the fact that a large number of $Ti_3C_2T_x$ nanosheets interweave in cross-linking CNF networks and wrap on CNF and $Ti_3C_2T_x$ nanosheets which overlap with each other, promoting the construction of highly conductive networks. The porous structures of TCTA improve the impedance matching characteristics and facilitate electromagnetic waves to enter the interior of TCTA/epoxy nanocomposites. When electromagnetic waves strike on TCTA/epoxy nanocomposites, a portion of the electromagnetic waves is reflected due to impedance mismatch. Transmitted electromagnetic waves will further be converted into thermal energy due to strong electric loss by interaction between

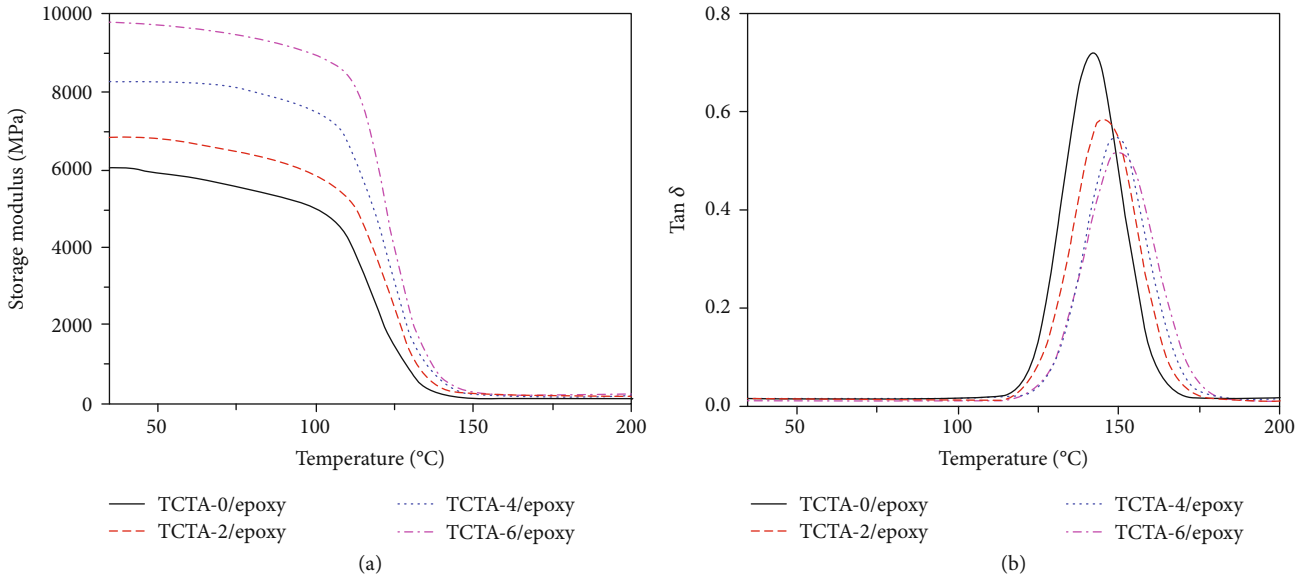

Figure 7: (a) Storage modulus *vs.* temperature and (b) Tanδ *vs.* temperature of the TCTA/epoxy nanocomposites.

electromagnetic waves and massive microcurrents in conductive networks [55]. Unique porous structures own large specific surface area and abundant interfaces. Due to interfacial polarization, local capacitive-like structures are induced by a large number of dipoles, enhancing the dielectric loss to electromagnetic waves. Moreover, the porous structures prolong the transmission paths of the electromagnetic waves by multiple reflection or scattering and further promote the reabsorption of the electromagnetic waves, which enhance the EMI SE values. In addition, the surface groups and defects of TCTA are beneficial to the attenuation of the electromagnetic waves owing to strengthened space charge polarization under the alternating electromagnetic field. The schematic diagram of the shielding mechanism for TCTA/epoxy nanocomposites is illustrated in Figures 5(f) and S9. Therefore, the absorption plays the key role in shielding mechanism for TCTA/epoxy nanocomposites.

Figure 7 shows the DMA curves of TCTA/epoxy nanocomposites. In Figure 7(a), as the temperature increases, the nanocomposites gradually change from the glassy state to the elastic state with a decrease of the storage modulus. The storage modulus of TCTA-0/epoxy nanocomposites in the glassy state is only 6039.0 MPa, whereas the storage modulus of TCTA-6/epoxy nanocomposites (1.38 vol% $Ti_3C_2T_x$) reaches 9792.5 MPa with an improvement of 62%. In addition, the glass transition temperature (T_g) also increases from 141.9°C to 150.3°C for TCTA-0/ and TCTA-6/epoxy nanocomposites, respectively, due to the strong interaction between $Ti_3C_2T_x$ and epoxy. TGA results in Figure S10 and Table S4 indicate that the residues of TCTA/epoxy nanocomposites gradually grow with an increase of the volume fraction of $Ti_3C_2T_x$, and the corresponding $T_{\text{Heat-resistance index}}$ (T_{HRI}) increases from 303.8°C to 310.7°C for TCTA-0/ and TCTA-6/epoxy nanocomposites [56], respectively, demonstrating that the incorporation of $Ti_3C_2T_x$ can enhance the thermal stabilities of the nanocomposites.

3. Discussion

3D highly conductive TCTA are assembled by directional freezing and freeze-drying method. After impregnating with epoxy resins, percolation threshold of $Ti_3C_2T_x$ in TCTA/epoxy nanocomposites is only 0.20 vol%. And when the volume fraction of $Ti_3C_2T_x$ is 1.38 vol%, the σ, EMI SE, and SE/d values of the TCTA-6/epoxy nanocomposites reach 1672 S/m, 74 dB, and 37 dB mm^{-1}, respectively, almost the optimal results compared to those of previously reported polymer nanocomposites. Owing to highly conductive porous networks, absorption dominates the shielding mechanism. In addition, the storage modulus and T_{HRI} values of TCTA-6/epoxy nanocomposites are enhanced to 9792.5 MPa and 310.7°C, increased by 62% and 6.9°C, respectively, compared to those of TCTA-0/epoxy nanocomposites. Our fabricated lightweight, easy-to-process, and shapeable TCTA/epoxy nanocomposites with superior EMI shielding performance, mechanical properties, and thermal stabilities will greatly widen the applications of MXene nanomaterials and epoxy resins in the field of high-tech EMI shielding.

4. Materials and Methods

Experimental details including $Ti_3C_2T_x$ synthesis, fabrication of TCTA and TCTA/epoxy nanocomposites, and characterizations can be found in Supplementary 1.

Conflicts of Interest

The authors declare that there are no conflicts of interest regarding the publication of this article.

Authors' Contributions

L. Wang conceived the project. L. Wang and P. Song conducted the synthesis, XRD, and EMI tests. All the authors

analyzed, discussed the data, and participated in writing the manuscript.

Acknowledgments

The authors are grateful for the support and funding from the Foundation of National Natural Science Foundation of China (51973173), the Natural Science Basic Research Plan for Distinguished Young Scholars in Shaanxi Province of China (2019JC-11), the Fundamental Research Funds for the Central Universities (310201911py010), and the Space Supporting Fund from China Aerospace Science and Industry Corporation (2019-HT-XG). L. Wang would like to thank the Innovation Foundation for Doctor Dissertation of Northwestern Polytechnical University (CX202053). We would like to thank the Analytical & Testing Center of Northwestern Polytechnical University for TEM and SEM tests.

Supplementary Materials

Supplementary 1. Figure S1: SEM image and wide-scan XPS spectrum of Ti_3AlC_2; wide-scan XPS spectrum, AFM image, and FTIR spectrum of $Ti_3C_2T_x$. Figure S2: SEM image of TCTA-0. Figure S3: cell size and distribution of TCTA. Figure S4: wide-scan XPS spectra of TCTA-0 and TCTA-6. Figure S5: Ti 2p spectra of $Ti_3C_2T_x$. Figure S6: σ values for TCTA and TCTA/epoxy nanocomposites. Figure S7: digital photographs showing LED lamp with TCTA-6/epoxy nanocomposites. Figure S8: EMI SE values of TCTA-6, TCTA-6/epoxy nanocomposites, and epoxy nanocomposites fabricated by blend-casting method. Figure S9: interaction between electromagnetic waves and TCTA/epoxy nanocomposites. Figure S10: TGA curves of the TCTA/epoxy nanocomposites. Table S1: comparison of electrical conductivities for TCTA with different densities. Table S2: comparison of EMI SE values for TCTA/epoxy nanocomposites. Table S3: comparison of EMI SE values of the TCTA/epoxy nanocomposites with other works. Table S4: thermal parameters of the TCTA/epoxy nanocomposites. *(Supplementary Materials)*

References

[1] C. Wang, V. Murugadoss, J. Kong et al., "Overview of carbon nanostructures and nanocomposites for electromagnetic wave shielding," *Carbon*, vol. 140, pp. 696–733, 2018.

[2] Y. Zhang, Y. Huang, T. Zhang et al., "Broadband and tunable high-performance microwave absorption of an ultralight and highly compressible graphene foam," *Advanced Materials*, vol. 27, no. 12, pp. 2049–2053, 2015.

[3] Z. Ling, C. E. Ren, M. Q. Zhao et al., "Flexible and conductive MXene films and nanocomposites with high capacitance," *Proceedings of the National Academy of Sciences*, vol. 111, no. 47, pp. 16676–16681, 2014.

[4] P. Xie, Z. Zhang, Z. Wang, K. Sun, and R. Fan, "Targeted double negative properties in silver/silica random metamaterials by precise control of microstructures," *Research*, vol. 2019, article 1021368, 11 pages, 2019.

[5] B. Shen, Y. Li, W. Zhai, and W. Zheng, "Compressible graphene-coated polymer foams with ultralow density for adjustable electromagnetic interference (EMI) shielding," *ACS Applied Materials & Interfaces*, vol. 8, no. 12, pp. 8050–8057, 2016.

[6] X. B. Xu, Z. M. Li, L. Shi, X. C. Bian, and Z. D. Xiang, "Ultralight conductive carbon-nanotube–polymer composite," *Small*, vol. 3, no. 3, pp. 408–411, 2007.

[7] D. X. Yan, H. Pang, B. Li et al., "Structured reduced graphene oxide/polymer composites for ultra-efficient electromagnetic interference shielding," *Advanced Functional Materials*, vol. 25, no. 4, pp. 559–566, 2015.

[8] L. Wang, H. Qiu, P. Song et al., "3D $Ti_3C_2T_x$ MXene/C hybrid foam/epoxy nanocomposites with superior electromagnetic interference shielding performances and robust mechanical properties," *Composites Part A: Applied Science and Manufacturing*, vol. 123, pp. 293–300, 2019.

[9] N. Li, Y. Huang, F. Du et al., "Electromagnetic interference (EMI) shielding of single-walled carbon nanotube epoxy composites," *Nano Letters*, vol. 6, no. 6, pp. 1141–1145, 2006.

[10] J. Liang, Y. Wang, Y. Huang et al., "Electromagnetic interference shielding of graphene/epoxy composites," *Carbon*, vol. 47, no. 3, pp. 922–925, 2009.

[11] V. Eswaraiah, V. Sankaranarayanan, and S. Ramaprabhu, "Functionalized graphene–pvdf foam composites for EMI shielding," *Macromolecular Materials and Engineering*, vol. 296, no. 10, pp. 894–898, 2011.

[12] N. Yousefi, X. Sun, X. Lin et al., "Highly aligned graphene/polymer nanocomposites with excellent dielectric properties for high-performance electromagnetic interference shielding," *Advanced Materials*, vol. 26, no. 31, pp. 5480–5487, 2014.

[13] Y. Guo, L. Pan, X. Yang et al., "Simultaneous improvement of thermal conductivities and electromagnetic interference shielding performances in polystyrene composites via constructing interconnection oriented networks based on electrospinning technology," *Composites Part A: Applied Science and Manufacturing*, vol. 124, article 105484, 2019.

[14] L. Q. Zhang, S. G. Yang, L. Li et al., "Ultralight cellulose porous composites with manipulated porous structure and carbon nanotube distribution for promising electromagnetic interference shielding," *ACS Applied Materials & Interfaces*, vol. 10, no. 46, pp. 40156–40167, 2018.

[15] P. Song, H. Qiu, L. Wang et al., "Honeycomb structural rGO-MXene/epoxy nanocomposites for superior electromagnetic interference shielding performance," *Sustainable Materials and Technologies*, vol. 24, article e00153, 2020.

[16] H. Pang, L. Xu, D. X. Yan, and Z. M. Li, "Conductive polymer composites with segregated structures," *Progress in Polymer Science*, vol. 39, no. 11, pp. 1908–1933, 2014.

[17] K. Zhang, G. H. Li, L. M. Feng et al., "Ultralow percolation threshold and enhanced electromagnetic interference shielding in poly (L-lactide)/multi-walled carbon nanotube nanocomposites with electrically conductive segregated networks," *Journal of Materials Chemistry C*, vol. 5, no. 36, pp. 9359–9369, 2017.

[18] Y. Chen, H. B. Zhang, Y. Yang, M. Wang, A. Cao, and Z. Z. Yu, "High-performance epoxy nanocomposites reinforced with three-dimensional carbon nanotube sponge for electromagnetic interference shielding," *Advanced Functional Materials*, vol. 26, no. 3, pp. 447–455, 2016.

[19] R. Sun, H. B. Zhang, J. Liu et al., "Highly conductive transition metal carbide/carbonitride(MXene)@polystyrene nanocomposites fabricated by electrostatic assembly for highly efficient electromagnetic interference shielding," *Advanced Functional Materials*, vol. 27, no. 45, article 1702807, 2017.

[20] W. Dai, J. Yu, Y. Wang et al., "Enhanced thermal conductivity for polyimide composites with a three-dimensional silicon carbide nanowire@graphene sheets filler," *Journal of Materials Chemistry A*, vol. 3, no. 9, pp. 4884–4891, 2015.

[21] C. Shao, Y. Liu, J. Chi, J. Wang, Z. Zhao, and Y. Zhao, "Responsive inverse opal scaffolds with biomimetic enrichment capability for cell culture," *Research*, vol. 2019, article 9783793, 10 pages, 2019.

[22] Y.-J. Wan, P.-L. Zhu, S.-H. Yu, R. Sun, C.-P. Wong, and W.-H. Liao, "Anticorrosive, ultralight, and flexible carbon-wrapped metallic nanowire hybrid sponges for highly efficient electromagnetic interference shielding," *Small*, vol. 14, no. 27, article 1800534, 2018.

[23] J. Liu, H. B. Zhang, X. Xie et al., "Multifunctional, superelastic, and lightweight MXene/polyimide aerogels," *Small*, vol. 14, no. 45, article 1802479, 2018.

[24] K. S. Kumar, P.-Y. Chen, and H. Ren, "A review of printable flexible and stretchable tactile sensors," *Research*, vol. 2019, article 3018568, 32 pages, 2019.

[25] Q. He, X. X. Liu, R. Wu, and J. S. Chen, "PVP-assisted synthesis of self-supported Ni_2P@carbon for high-performance supercapacitor," *Research*, vol. 2019, article 8013285, 10 pages, 2019.

[26] J. Ling, W. Zhai, W. Feng, B. Shen, J. Zhang, and W. . Zheng, "Facile preparation of lightweight microcellular polyetherimide/graphene composite foams for electromagnetic interference shielding," *ACS Applied Materials & Interfaces*, vol. 5, no. 7, pp. 2677–2684, 2013.

[27] H. Xu, X. Yin, X. Li et al., "Lightweight Ti2CTxMXene/poly(-vinyl alcohol) composite foams for electromagnetic wave shielding with absorption-dominated feature," *ACS Applied Materials & Interfaces*, vol. 11, no. 10, pp. 10198–10207, 2019.

[28] X. Zhang, T. Zhang, Z. Wang et al., "Ultralight, superelastic, and fatigue-resistant graphene aerogel templated by graphene oxide liquid crystal stabilized air bubbles," *ACS Applied Materials & Interfaces*, vol. 11, no. 1, pp. 1303–1310, 2018.

[29] T. Liu, M. Huang, X. Li, C. Wang, C. X. Gui, and Z. Z. Yu, "Highly compressible anisotropic graphene aerogels fabricated by directional freezing for efficient absorption of organic liquids," *Carbon*, vol. 100, pp. 456–464, 2016.

[30] G. Yu, A. Cao, and C. M. Lieber, "Large-area blown bubble films of aligned nanowires and carbon nanotubes," *Nature Nanotechnology*, vol. 2, no. 6, pp. 372–377, 2007.

[31] X.-H. Li, X. Li, K.-N. Liao et al., "Thermally annealed anisotropic graphene aerogels and their electrically conductive epoxy composites with excellent electromagnetic interference shielding efficiencies," *ACS Applied Materials & Interfaces*, vol. 8, no. 48, pp. 33230–33239, 2016.

[32] Z. Zeng, H. Jin, M. Chen, W. Li, L. Zhou, and Z. Zhang, "Lightweight and anisotropic porous MWCNT/WPU composites for ultrahigh performance electromagnetic interference shielding," *Advanced Functional Materials*, vol. 26, no. 2, pp. 303–310, 2016.

[33] C. Liang, H. Qiu, P. Song, X. Shi, J. Kong, and J. Gu, "Ultralight mxene aerogel/wood-derived porous carbon composites with wall-like "mortar/brick" structures for electromagnetic interference shielding," *Science Bulletin*, vol. 65, no. 8, pp. 616–622, 2020.

[34] J. Song, C. Chen, Z. Yang et al., "Highly compressible, anisotropic aerogel with aligned cellulose nanofibers," *ACS Nano*, vol. 12, no. 1, pp. 140–147, 2018.

[35] T. Ma, Y. Zhao, K. Ruan et al., "Highly thermal conductivities, excellent mechanical robustness and flexibility, and outstanding thermal stabilities of aramid nanofiber composite papers with nacre-mimetic layered structures," *ACS Applied Materials & Interfaces*, vol. 12, no. 1, pp. 1677–1686, 2019.

[36] Z.-Y. Wu, P. Yin, H.-X. Ju et al., "Natural nanofibrous cellulose-derived solid acid catalysts," *Research*, vol. 2019, article 6262719, 11 pages, 2019.

[37] B. Ahmed, D. H. Anjum, Y. Gogotsi, and H. N. Alshareef, "Atomic layer deposition of SnO_2 on MXene for Li-ion battery anodes," *Nano Energy*, vol. 34, pp. 249–256, 2017.

[38] Y. Zhang, L. Wang, J. Zhang et al., "Fabrication and investigation on the ultra-thin and flexible $Ti_3C_2T_x$/co-doped polyaniline electromagnetic interference shielding composite films," *Composites Science and Technology*, vol. 183, article 107833, 2019.

[39] C. Zhu, E. Chalmers, L. Chen et al., "A nature-inspired, flexible substrate strategy for future wearable electronics," *Small*, vol. 15, no. 35, article 1902440, 2019.

[40] X. Yang, S. Fan, Y. Li et al., "Synchronously improved electromagnetic interference shielding and thermal conductivity for epoxy nanocomposites by constructing 3D copper nanowires/thermally annealed graphene aerogel framework," *Composites Part A: Applied Science and Manufacturing*, vol. 128, article 105670, 2020.

[41] P. Wu, Z. Fang, A. Zhang et al., "Chemically binding scaffolded anodes with 3D graphene architectures realizing fast and stable lithium storage," *Research*, vol. 2019, article 8393085, 9 pages, 2019.

[42] M. Naguib, V. N. Mochalin, M. W. Barsoum, and Y. Gogotsi, "25th anniversary article: MXenes: a new family of two-dimensional materials," *Advanced Materials*, vol. 26, no. 7, pp. 992–1005, 2014.

[43] W. Dai, L. Lv, J. Lu et al., "A paper-like inorganic thermal interface material composed of hierarchically structured graphene/silicon carbide nanorods," *ACS Nano*, vol. 13, no. 2, pp. 1547–1554, 2019.

[44] X. Chen, F. Meng, Z. Zhou et al., "One-step synthesis of graphene/polyaniline hybrids by in situ intercalation polymerization and their electromagnetic properties," *Nanoscale*, vol. 6, no. 14, pp. 8140–8148, 2014.

[45] Z. Na, R. Yao, Q. Yan, X. Sun, and G. Huang, "General growth of carbon nanotubes for cerium redox reactions in high-efficiency redox flow batteries," *Research*, vol. 2019, article 3616178, 12 pages, 2019.

[46] M. Hu, Z. Li, T. Hu, S. Zhu, C. Zhang, and X. Wang, "High-capacitance mechanism for $Ti_3C_2T_x$MXene by in situ electrochemical Raman spectroscopy investigation," *ACS Nano*, vol. 10, no. 12, pp. 11344–11350, 2016.

[47] Y. Mo, J. Liu, S. Wang et al., "Low-carbon and nanosheathed ZnCo2O4Spheroids with porous architecture for boosted lithium storage properties," *Research*, vol. 2019, article 1354829, 11 pages, 2019.

[48] L. Wang, H. Qiu, C. Liang et al., "Electromagnetic interference shielding MWCNT-Fe_3O_4@Ag/epoxy nanocomposites with satisfactory thermal conductivity and high thermal stability," *Carbon*, vol. 141, pp. 506–514, 2019.

[49] M. Naguib, T. Saito, S. Lai et al., "$Ti_3C_2T_x$ (MXene)–polyacrylamide nanocomposite films," *RSC Advances*, vol. 6, no. 76, pp. 72069–72073, 2016.

[50] S. Vadukumpully, J. Paul, N. Mahanta, and S. Valiyaveettil, "Flexible conductive graphene/poly (vinyl chloride) composite

thin films with high mechanical strength and thermal stability," *Carbon*, vol. 49, no. 1, pp. 198–205, 2011.

[51] S.-T. Hsiao, C.-C. M. Ma, W.-H. Liao et al., "Lightweight and flexible reduced graphene oxide/water-borne polyurethane composites with high electrical conductivity and excellent electromagnetic interference shielding performance," *ACS Applied Materials & Interfaces*, vol. 6, no. 13, pp. 10667–10678, 2014.

[52] S. Zhao, H. B. Zhang, J. Q. Luo et al., "Highly electrically conductive three-dimensional $Ti_3C_2T_x$MXene/reduced graphene oxide hybrid aerogels with excellent electromagnetic interference shielding performances," *ACS Nano*, vol. 12, no. 11, pp. 11193–11202, 2018.

[53] C. Wu, X. Huang, G. Wang et al., "Highly conductive nanocomposites with three-dimensional, compactly interconnected graphene networks via a self-assembly process," *Advanced Functional Materials*, vol. 23, no. 4, pp. 506–513, 2013.

[54] Z. Chen, C. Xu, C. Ma, W. Ren, and H. M. Cheng, "Lightweight and flexible graphene foam composites for high-performance electromagnetic interference shielding," *Advanced Materials*, vol. 25, no. 9, pp. 1296–1300, 2013.

[55] L. Wang, X. Shi, J. Zhang, Y. Zhang, and J. Gu, "Lightweight and robust rGO/sugarcane derived hybrid carbon foams with outstanding EMI shielding performance," *Journal of Materials Science & Technology*, vol. 52, pp. 119–126, 2020.

[56] Y. Han, X. Shi, X. Yang et al., "Enhanced thermal conductivities of epoxy nanocomposites via incorporating in- situ fabricated hetero-structured SiC-BNNS fillers," *Composites Science and Technology*, vol. 187, article 107944, 2020.